Article

Influence of the Initial Prestress Level on the Distribution of Regions of Dynamic Instability of Geiger Domes

Paulina Obara [ID] and Maryna Solovei *[ID]

Faculty of Civil Engineering and Architecture, Kielce University of Technology, al. Tysiąclecia Państwa Polskiego 7, 25-314 Kielce, Poland; paula@tu.kielce.pl
* Correspondence: msolovei@tu.kielce.pl

Abstract: This paper provides a parametric analysis of cable–strut tensegrity domes subjected to periodic loads. This analysis aims at determining the main regions of dynamic instability (unstable regions). From the point of view of the physical interpretation of the phenomenon, if the load occurs in these regions, the amplitudes of the resulting vibrations increase, posing a risk to the durability of the structures. The consideration includes cable–strut structures called Geiger domes. Four dome design solutions known from the literature are compared, i.e., regular (patented by Geiger) and modified domes with a closed and an open upper section. In contrast to conventional cable–strut structures, Geiger domes are characterized by a self-equilibrated system of internal forces (initial prestress), which affects the shape and range of unstable regions. The main purpose is to answer the question as to which type of design solution is more sensitive to the risk of excitation vibrations. A nondimensional parameter λ is introduced for this quantitative assessment. This parameter reliably determines the change in the area of unstable regions as the initial prestress level increases. The range of the parameter λ is defined as a value between 1 and 0. In the case of $\lambda = 1$, there is potential for the excitation of unstable motion, whereas in the case of $\lambda = 0$, such a risk is absent. The analysis presented in this paper can be employed in the process of optimizing the initial prestress level, which will constitute the subsequent stage of this research. A geometrically non-linear model is used to evaluate the behavior of the considered structures.

Keywords: Geiger dome; initial prestress; infinitesimal mechanism; resonance frequency; unstable region

1. Introduction

This paper concerns a dynamic instability analysis of strut–cable domes called Geiger domes. The origins of these structures date back to David Geiger's 1988 patent [1] on roof construction. This solution is considered the first tensegrity dome. A characteristic feature of the Geiger domes is the occurrence of several, dozen, or several dozen infinitesimal mechanisms and a self-equilibrated system of internal forces (initial prestress). In the absence of initial prestress, the domes are unstable, i.e., geometrically variable. The stabilization occurs only when the initial prestress is introduced.

Geiger's solutions were implemented on the roof of Olympic Hall in Seoul [2] in 1988. Geiger domes have been the subject of many theoretical and experimental scientific works. From the beginning of the idea to the present day, new topologies based on the original patent were created via different form-finding methods, for example, the dual use of singular value decomposition (DSVD) [3], the genetic algorithm [4], the force density method [5], the unbalanced force iteration method [6], the modified fractional-step finite element method [7], the catenary-equation-based component force balancing method [8], and the optimization approach [9]. Due to the unconventional shape and unique features of tensegrity domes, parametric analyses considering the effect of the initial prestress on behavior is very important. The effect of the initial prestress on the mechanical properties,

i.e., displacement and stiffness, among others, has been investigated in [10–13]. In turn, the dynamic responses to changes in the initial prestress are presented in [14–18].

To the best of our knowledge, despite the many studies on Geiger domes, there has been no analysis of dynamic stability, or "dynamic instability", understood in terms of the Bolotin approach [19,20]. From the perspective of structural durability, dynamic instability analysis is of significant importance. This process allows for the identification of the boundaries of instability, which are commonly referred to as Ince–Strutt maps or parametric resonance regions in the literature. These regions are distinguished by the excitation of unstable motion. From a mathematical point of view, the concept of stable and unstable regions corresponds to the solutions of non-linear parametric equations of motion, also known as Mathieu equations [21]. The finite solutions correspond to stable regions, whereas the solutions that increase indefinitely in time are indicative of unstable regions. The fundamental issues have been clearly delineated [19,20,22]; however, it is still a very popular topic [23,24].

This paper investigates the dynamic instability of Geiger domes. Four design solutions known from the literature are taken into account. The main purpose of this paper is to answer the question as to which type of design solution is more sensitive to the risk of excitation vibrations. For this purpose, unstable regions as a function of the initial prestress are determined. The stability charts of the Mathieu equations are calculated using the harmonic balance method [19,20,22,23,25]. For the quantitative assessment of the changes in unstable regions as the initial prestress level increases, a dimensionless parameter is introduced. This parameter measures the changes in the areas of unstable regions as the initial prestress level increases.

The rest of this paper is organized as follows: Section 2 describes a discrete model of the Geiger dome, including a description of the stiffness of the structures and the mathematical description needed to determine the main unstable regions. In Section 3, the results obtained for four different design solutions of Geiger domes from the literature are presented. A non-linear analysis is used, assuming the hypothesis of large displacements [16,25,26]. The analyses were performed in an original program written in the Mathematica environment. This program allows for obtaining diagrams in which the unstable regions are located as functions of the dynamic force applied and vibration frequency of the considered structures, taking into account the influence of the initial prestress. Finally, in Section 4, some conclusions are drawn.

2. Methods of Analysis

Dynamic instability analysis leads to the identification of the resonance frequencies of periodic loads and, consequently, to the determination of parametric resonance regions (unstable regions). The analysis of unstable regions at a periodic load

$$P(t) = P + P_t\cos(\theta t) \tag{1}$$

is carried out, where P is a constant value of the load, P_t is the amplitude of the load, and θ is the frequency of the load. The main unstable regions, i.e., periodic resonances of the first order, are identified. The influence of initial prestress on the shape and range of unstable regions is considered. The discrete formulation with the finite element method is used.

2.1. Discrete Model of Geiger Dome

The components of Geiger domes are modeled as a space finite tensegrity element e of Young's modulus E_e, density ρ_e, cross-sectional area A_e, and length L_e (Figure 1). This element is described by the elongation matrix

$$\mathbf{B}^e = \begin{bmatrix} -c_x & -c_y & -c_z & c_x & c_y & c_z \end{bmatrix} \in \mathbb{R}^{1\times 6}, \tag{2}$$

where

$$c_x = \frac{L_{ex}}{L_e}, c_y = \frac{L_{ey}}{L_e}, c_z = \frac{L_{ez}}{L_e}$$

are the directional cosines, where $L_{ex} = x_{n_2} - x_{n_1}$, $L_{ex} = y_{n_2} - y_{n_1}$, and $L_{ex} = z_{n_2} - z_{n_1}$. Additionally, the inclusion of the initial stress σ_0 is considered, and the influences of the external load on the static and dynamic behavior of the structure are considered. We take into account the following matrices describing the element:

$$\mathbf{K}_L^e = \frac{E_e A_e}{L_e} \begin{bmatrix} \mathbf{I}_0 & -\mathbf{I}_0 \\ -\mathbf{I}_0 & \mathbf{I}_0 \end{bmatrix}, \quad \mathbf{K}_G^e = \frac{A_e \sigma_0}{L_e} \begin{bmatrix} \mathbf{I} & -\mathbf{I} \\ -\mathbf{I} & \mathbf{I} \end{bmatrix}, \quad \mathbf{K}_{GN}^e = \frac{N_e}{L_e} \begin{bmatrix} \mathbf{I} & -\mathbf{I} \\ -\mathbf{I} & \mathbf{I} \end{bmatrix}$$
$$\mathbf{K}_{NL}^e = \frac{E_e A_e}{L_e^2} \begin{bmatrix} \mathbf{I}_1 & -\mathbf{I}_1 \\ -\mathbf{I}_1 & \mathbf{I}_1 \end{bmatrix} + \frac{E_e A_e}{L_e^3} \begin{bmatrix} \mathbf{I}_2 & -\mathbf{I}_2 \\ -\mathbf{I}_2 & \mathbf{I}_2 \end{bmatrix}, \quad \mathbf{M}^e = \frac{\rho_e A_e l_e}{6} \begin{bmatrix} 2\mathbf{I} & \mathbf{I} \\ \mathbf{I} & 2\mathbf{I} \end{bmatrix},$$

(3)

where $\mathbf{K}_L^e \in \mathbb{R}^{6\times6}$ is a linear stiffness matrix, $\mathbf{K}_G^e \in \mathbb{R}^{6\times6}$ is a geometric stiffness matrix depending on the initial stress σ_0, $\mathbf{K}_{GN}^e \in \mathbb{R}^{6\times6}$ is a geometric stiffness matrix depending on the axial forces that result from the external load, $\mathbf{K}_{NL}^e \in \mathbb{R}^{6\times6}$ is a non-linear stiffness matrix, $\mathbf{M}^e \in \mathbb{R}^{6\times6}$ is a consistent mass matrix, and

$$\mathbf{I} = \begin{bmatrix} 1 & 0 & 0 \\ 0 & 1 & 0 \\ 0 & 0 & 1 \end{bmatrix}, \mathbf{I}_0 = \begin{bmatrix} 1 & 0 & 0 \\ 0 & 0 & 0 \\ 0 & 0 & 0 \end{bmatrix}, \mathbf{I}_1 = \begin{bmatrix} 2\Delta_{u_1} & \Delta_{u_2} & \Delta_{u_2} \\ \Delta_{u_2} & 0 & 0 \\ \Delta_{u_2} & 0 & 0 \end{bmatrix}, \mathbf{I}_2 = \begin{bmatrix} (\Delta_{u_1})^2 & \Delta_{u_1}\Delta_{u_2} & \Delta_{u_1}\Delta_{u_2} \\ \Delta_{u_1}\Delta_{u_2} & (\Delta_{u_2})^2 & \Delta_{u_2}\Delta_{u_2} \\ \Delta_{u_1}\Delta_{u_2} & \Delta_{u_2}\Delta_{u_2} & (\Delta_{u_2})^2 \end{bmatrix}$$

where $\Delta_{u_i} = q_i^{(n_2)} - q_i^{(n_1)} (i = 1, 2, 3)$ are the displacement increases between nodes of the element, i.e., $q_i^{(n_2)}$ is a displacement of second node, and $q_i^{(n_1)}$ is a displacement of the first node (Figure 1).
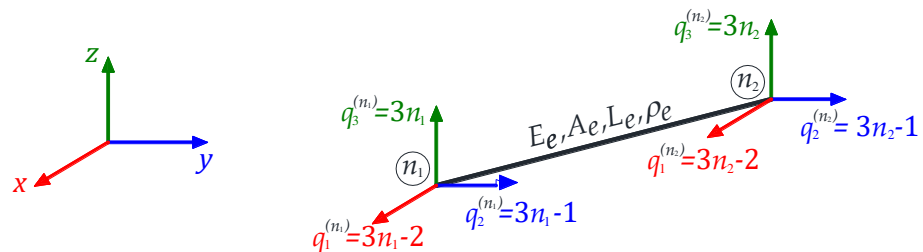

Figure 1. Global degrees of freedom of a space finite tensegrity element.

The *n*-element structures ($e = 1, 2, \ldots, n$) with *m* degrees of freedom described by a displacement vector $\mathbf{q}(t)$ and loaded by forces applied at the nodes **P** are considered:

$$\mathbf{q}(t) = \begin{bmatrix} q_1 & q_2 & \ldots & q_m \end{bmatrix}^T \in \mathbb{R}^{m\times1}, \qquad \mathbf{P} = \begin{bmatrix} P_1 & P_2 & \ldots & P_m \end{bmatrix}^T \in \mathbb{R}^{m\times1}.$$ (4)

The elasticity of the structures is described by an elasticity matrix

$$\mathbf{E} = diag \begin{bmatrix} \frac{E_1 A_1}{L_1} & \frac{E_2 A_2}{L_2} & \ldots & \frac{E_n A_n}{L_n} \end{bmatrix} \in \mathbb{R}^{n\times n},$$ (5)

whereas the other matrices describing the structure, i.e., $\mathbf{B} \in \mathbb{R}^{n\times m}$, $\mathbf{K}_L \in \mathbb{R}^{m\times m}$, $\mathbf{K}_G \in \mathbb{R}^{m\times m}$, $\mathbf{K}_{NL} \in \mathbb{R}^{m\times m}$, and $\mathbf{M} \in \mathbb{R}^{m\times m}$, are determined using finite element formalism [27,28].

2.2. Stiffness of Geiger Domes

Geiger domes are characterized by the occurrence of two immanent features of tensegrity structures, i.e., an infinitesimal mechanism and a self-stress state. Both of these features depend only on the configuration of the elements, which is described by the nondimensional elongation matrix **B**. The infinitesimal mechanism $\mathbf{x}_S \in \mathbb{R}^{n\times1}$ is an eigenvector re-

lated to the zero eigenvalue of the matrix $\mathbf{B}^T\mathbf{B} \in \mathbb{R}^{m \times m}$, whereas the self-stress state vector $\mathbf{y}_S \in \mathbb{R}^{n \times 1}$ is an eigenvector related to the zero eigenvalue of the matrix $\mathbf{BB}^T \in \mathbb{R}^{n \times n}$ [13,18]. In the absence of the self-stress state (initial prestress), Geiger domes are unstable. The stabilization occurs only when the initial prestress forces are introduced:

$$\mathbf{S} = \mathbf{y}_s S \in \mathbb{R}^{n \times 1}. \tag{6}$$

where S is an initial prestress level.

In analysis, a very important aspect is the determination of the prestress range, i.e., the minimum S_{min} and maximum S_{max} levels of the initial prestress. The initial prestress level in each structure is unique and depends on the design assumptions and external loads. Geiger domes consist of two types of elements, i.e., struts, which are responsible for carrying compressive prestress, and cables, which are responsible for carrying tensile prestress. The external load causes additional prestress of the structure. However, this can also lead to an incorrect redistribution of the normal forces, which must be corrected by the implementation of an appropriate initial prestress level. On the other hand, the load-bearing capacity must be ensured; that is, the permissible stresses must not be exceeded. This means that

- The minimum prestress level S_{min} is related to an appropriate redistribution of the normal forces;
- The maximum prestress level S_{max} is related to the load-bearing capacity of the most stressed element.

It is of significant importance to consider the initial prestress in order to stabilize Geiger domes and prevent dynamic instability. However, the degree of stabilization also depends on the external load. Accordingly, the geometric stiffness (the initial stress matrix) $\mathbf{K}_G$ should be calculated as follows:

$$\mathbf{K}_G = [\mathbf{K}_G(\mathbf{S}) + \mathbf{K}_{GN}(\mathbf{N})] \in \mathbb{R}^{m \times m}, \tag{7}$$

where $\mathbf{K}_G(\mathbf{S})$ is the part depending on the self-equilibrated internal forces (6). In turn, $\mathbf{K}_{GN}(\mathbf{N})$ is the part depending on the axial forces N_e ($\mathbf{N} = \begin{bmatrix} N_1 & N_2 & \ldots N_n \end{bmatrix} \in \mathbb{R}^{n \times 1}$) that result from the external load, calculated using non-linear analysis:

$$[\mathbf{K}_L + \mathbf{K}_G(\mathbf{S}) + \mathbf{K}_{NL}(\mathbf{q})]\mathbf{q} = \mathbf{P}, \tag{8}$$

where $\mathbf{K}_L \in \mathbb{R}^{m \times m}$ is a linear stiffness matrix, and $\mathbf{K}_{NL}(\mathbf{q}) \in \mathbb{R}^{m \times m}$ is a non-linear displacement stiffness matrix. The non-linear Equation (8), solved by an incremental–iterative analysis of large displacement gradients, consequently leads to real normal force in elements

$$N_e = E_e A_e \varepsilon_e \sqrt{1 + 2\varepsilon_e}, \tag{9}$$

where

$$\varepsilon_e = \frac{1}{2} \frac{(L_e^a)^2 - (L_e)^2}{(L_e)^2} \tag{10}$$

is the strain that depends on the length of an element in the actual configuration L_e^a:

$$L_e^a = \sqrt{(\Delta_{u_2})^2 + (\Delta_{u_3})^2 + (L_e + \Delta_{u_1})^2}. \tag{11}$$

The process for determining the stiffness of Geiger domes is shown in Figure 2. It should be noted that matrix $\mathbf{K}_{GN}(\mathbf{N})$ depends on both the external load $\mathbf{P}$ and the initial prestress $\mathbf{S}$. The initial prestress changes from S_{min} to S_{max}. From a design point of view, the most important is the process of optimizing [29] the initial prestress level. However, it requires a full spectrum of analysis, including that provided in this paper. Optimization is the next step in our considerations.
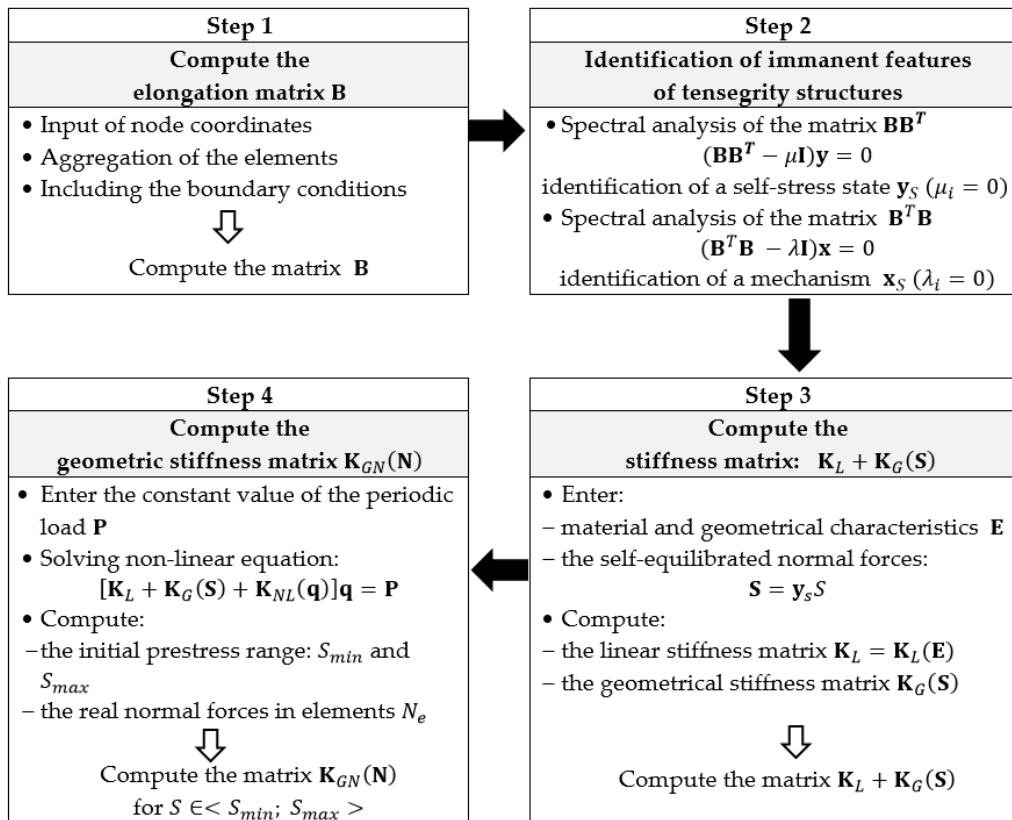
Step 1	Step 2
Compute the elongation matrix B	**Identification of immanent features of tensegrity structures**
• Input of node coordinates • Aggregation of the elements • Including the boundary conditions ⇩ Compute the matrix **B**	• Spectral analysis of the matrix $\mathbf{BB}^T$ $\qquad (\mathbf{BB}^T - \mu\mathbf{I})\mathbf{y} = 0$ identification of a self-stress state $\mathbf{y}_S$ ($\mu_i = 0$) • Spectral analysis of the matrix $\mathbf{B}^T\mathbf{B}$ $\qquad (\mathbf{B}^T\mathbf{B} - \lambda\mathbf{I})\mathbf{x} = 0$ identification of a mechanism $\mathbf{x}_S$ ($\lambda_i = 0$)

Step 4	Step 3
Compute the geometric stiffness matrix $\mathbf{K}_{GN}(\mathbf{N})$	**Compute the stiffness matrix: $\mathbf{K}_L + \mathbf{K}_G(\mathbf{S})$**
• Enter the constant value of the periodic load **P** • Solving non-linear equation: $\qquad [\mathbf{K}_L + \mathbf{K}_G(\mathbf{S}) + \mathbf{K}_{NL}(\mathbf{q})]\mathbf{q} = \mathbf{P}$ • Compute: – the initial prestress range: S_{min} and S_{max} – the real normal forces in elements N_e ⇩ Compute the matrix $\mathbf{K}_{GN}(\mathbf{N})$ for $S \in\, < S_{min};\, S_{max} >$	• Enter: – material and geometrical characteristics **E** – the self-equilibrated normal forces: $\qquad\qquad \mathbf{S} = \mathbf{y}_s S$ • Compute: – the linear stiffness matrix $\mathbf{K}_L = \mathbf{K}_L(\mathbf{E})$ – the geometrical stiffness matrix $\mathbf{K}_G(\mathbf{S})$ ⇩ Compute the matrix $\mathbf{K}_L + \mathbf{K}_G(\mathbf{S})$

Figure 2. Process for determining the stiffness of Geiger domes.

2.3. Dynamic Stability Analysis

In the general case, the study of the structural instability problems leads to non-linear issues, which are solved by iterative or incremental–iterative analysis of large displacement gradients. However, in the case of dynamic instability analysis, the nature of motion is studied. A quasi-linear approach is sufficient for determining the conditions under which the motion is of an unsteady nature, with solutions that increase indefinitely with time. Admittedly, the determination of the magnitude of the amplitudes of these oscillations can only be obtained from non-linear equations of vibration, no less; without knowing the magnitude of the amplitudes, quasi-linear theory gives a sufficiently complete and accurate view of the issue of instability. The equation of motion with time-varying coefficients with the inclusion of a periodic load (1) takes the following form:

$$\mathbf{M}\ddot{\mathbf{q}}(t) + [\mathbf{K}_L + \mathbf{K}_G(\mathbf{S}) + P(t)\mathbf{K}_{GN}(\mathbf{N})]\mathbf{q}(t) = 0, \tag{12}$$

where $\mathbf{M} \in \mathbb{R}^{m\times m}$ is a consistent mass matrix, and $\ddot{\mathbf{q}}(t) \in \mathrm{R}^{m\times 1}$ is an acceleration vector.

The boundaries of the stable and unstable regions (Ince–Strutt maps) are determined using the periodic solutions of the equation of motion (12). The problem of dynamic instability analysis leads to determining the conditions under which Equation (12) has nonzero solutions. In this paper, the dynamic instability analysis is carried out using the harmonic balance method (for a detailed description, see [23,25]). This method leads to the boundaries of the first, second, third, etc., resonance regions. The focus of this consideration is the first (main) resonance region. The equation sufficient to do this takes the following form:

$$\det\left\{\mathbf{K}_L + \mathbf{K}_G(\mathbf{S}) + \left(1 \pm \frac{1}{2}\frac{P_t}{P}\right)\mathbf{K}_{GN}(\mathbf{N}) - \frac{\theta^2}{4}\mathbf{M}\right\} = 0. \tag{13}$$

Based on Equation (13), the main unstable regions $A_\eta(S_i)$ for the i-th initial prestress level S_i are determined in the plane of a pulsatility index v and a resonance frequency η:

$$v = \frac{P_t}{P}, \quad \eta = \frac{\theta}{2\pi}. \tag{14}$$

For quantitative assessment, the nondimensional parameter

$$\lambda = \frac{A_\eta(S_i)}{A_\eta(S_{min})} \tag{15}$$

is introduced, which expresses the ratio of the area of the unstable region at the i-th level of initial prestress S_i to the area of the unstable region at the minimum initial prestress level S_{min}. The range of parameter λ is defined as a value between 1 and 0. In the case of $\lambda = 1$, there is the potential for the excitation of unstable motion, whereas in the case of $\lambda = 0$, such a risk is absent. Additionally, from the perspective of structural durability, the characteristics of the changes in the parameter with growth in the initial prestress level are important. The best solution is obtained when the parameter λ decreases exponentially as the initial prestress level increases.

2.4. Simplest Two-Element Cable Structure

The simplest two-dimensional structure is considered to explain in detail the process for determining the stiffness of the structures and the process of dynamic stability analysis. Despite the fact that it is not a tensegrity structure, its behavior fully reflects the behavior of tensegrity structures. This is because the structure is characterized by two inherent features of tensegrity systems, i.e., the self-stress state and an infinitesimal mechanism. For such a simple structure, it is possible to determine the stiffness and impact of the initial prestress level S on the unstable regions in explicit form. This approach makes it easier to understand the behavior of Geiger domes.

Step 1—Compute the elongation matrix

The truss, consisting of two elements ($n = 2$) with length l and stiffness EA, characterized by two degrees of freedom ($m = 2$), is considered (Figure 3a). A force P applied to the 2nd node in the vertical direction is taken into account (Figure 3b). The displacement vector $(4)_1$, vector of force $(4)_2$, and elongation matrix are as follows:

$$\mathbf{q} = \begin{bmatrix} q_1 \\ q_2 \end{bmatrix}, \quad \mathbf{P} = \begin{bmatrix} 0 \\ P \end{bmatrix}, \quad \mathbf{B} = \begin{bmatrix} 1 & 0 \\ -1 & 0 \end{bmatrix}. \tag{16}$$
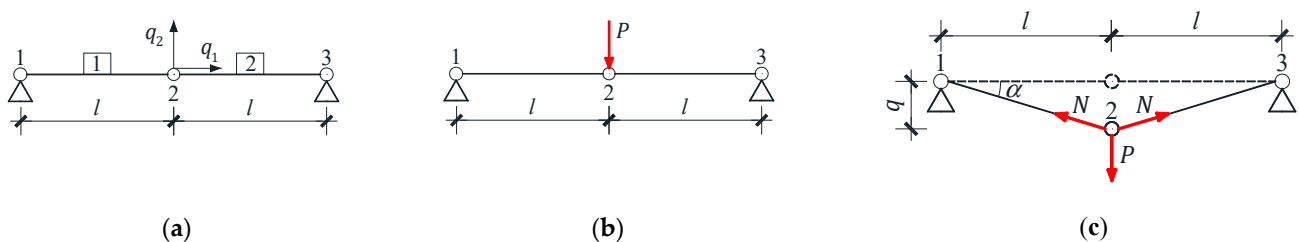

(a)   **(b)**   **(c)**

Figure 3. Two-element structure: (**a**) geometry, (**b**) scheme of loading regime, (**c**) actual configuration.

Step 2—Identification of immanent features of tensegrity structures

Spectral analysis of matrix $\mathbf{BB}^T$ leads to obtain two eigenvalues, one of which is zero ($\mu_2 = 0$). The zero eigenvalue is related to the existence of one self-stress state, considered as an eigenvector related to the zero eigenvalue:

$$\mathbf{BB}^T = \begin{bmatrix} 1 & -1 \\ -1 & 1 \end{bmatrix} \xrightarrow{(\mathbf{BB}^T - \mu\mathbf{I})\mathbf{y}=0} \boldsymbol{\mu} = \begin{bmatrix} 2 & 0 \end{bmatrix} \rightarrow \mathbf{y}_S = \mathbf{y}_2(\mu_2 = 0) = \begin{bmatrix} 1 \\ 1 \end{bmatrix}. \tag{17}$$

Spectral analysis of matrix $\mathbf{B}^T\mathbf{B}$ leads to obtaining two eigenvalues, one of which is also zero ($\lambda_2 = 0$). The zero eigenvalue is related to the existence of one mechanism considered as an eigenvector related to the zero eigenvalue:

$$\mathbf{B}^T\mathbf{B} = \begin{bmatrix} 2 & 0 \\ 0 & 0 \end{bmatrix} \overset{(\mathbf{B}^T\mathbf{B}-\lambda\mathbf{I})\mathbf{x}=0}{\longrightarrow} \lambda = \begin{bmatrix} 2 & 0 \end{bmatrix} \to \mathbf{x}_S = \mathbf{x}_2(\gamma_2 = 0) = \begin{bmatrix} 0 \\ 1 \end{bmatrix}. \tag{18}$$

Step 3—Compute the stiffness matrix $\mathbf{K}_L + \mathbf{K}_G(\mathbf{S})$

The elasticity matrix (5) and the self-equilibrated normal forces (6) are as follows:

$$\mathbf{E} = \frac{EA}{l} \begin{bmatrix} 1 & 0 \\ 0 & 1 \end{bmatrix}, \quad \mathbf{S} = S \begin{bmatrix} 1 \\ 1 \end{bmatrix}. \tag{19}$$

Due to this, the stiffness matrix takes the following form:

$$\mathbf{K}_L = \frac{2EA}{l} \begin{bmatrix} 1 & 0 \\ 0 & 0 \end{bmatrix}, \quad \mathbf{K}_G(\mathbf{S}) = \frac{2S}{l} \begin{bmatrix} 1 & 0 \\ 0 & 1 \end{bmatrix}. \tag{20}$$

Step 4—Compute the geometric stiffness matrix $\mathbf{K}_{GN}(\mathbf{N})$

The non-linear equation of a static equilibrium (8) for a considered truss takes the following form:

$$\left\{ \frac{2EA}{l} \begin{bmatrix} 1 & 0 \\ 0 & 0 \end{bmatrix} + \frac{2S}{l} \begin{bmatrix} 1 & 0 \\ 0 & 1 \end{bmatrix} + \frac{EA}{l^3} \begin{bmatrix} q_1^2 & q_1 q_2 \\ q_1 q_2 & q_2^2 \end{bmatrix} \right\} \begin{bmatrix} q_1 \\ q_2 \end{bmatrix} = \begin{bmatrix} 0 \\ -P \end{bmatrix}. \tag{21}$$

Due to the symmetry of the structure and load, the displacement q_1 is zero. To simplify the notation $q = -q_2$, Equation (21) takes the following form:

$$[S + N(P)]q = \frac{Pl}{2}, \tag{22}$$

where

$$N(P) = \frac{EA}{2}\left(\frac{q}{l}\right)^2 \tag{23}$$

is a longitudinal force caused by load P. This means that it is the geometric stiffness matrix $\mathbf{K}_{GN}(\mathbf{N}) \equiv N(P)$. It should be noted that for a considered structure, it is possible to obtain a formula for the longitudinal forces $N(P + S)$ generated jointly by the external load P and prestress forces S. It can be simply determined by the static equilibrium of the 2nd node in the actual configuration (Figure 3c). So, the geometric stiffness matrix $\mathbf{K}_{GN}(\mathbf{N}) \equiv N(P)$ can be expressed as

$$N(P) = \frac{P}{2\sin\alpha} - S; \quad \sin\alpha = \frac{q}{\sqrt{l^2 + q^2}}. \tag{24}$$

The application of non-linear theory takes into account the stiffening of the structure under the influence of an external load. The considered force stabilizes the mechanism. In the absence of initial prestress ($S = 0$ kN), Equation (22) results in the calculation of the displacement

$$q(S = 0) = \sqrt[3]{\frac{P}{EA}}l. \tag{25}$$

In turn, if the non-linear influence is neglected ($N(P) = 0$), the solution of Equation (22) results in the calculation of the displacement

$$q = \frac{Pl}{2S}, \tag{26}$$

which increases to infinity in the absence of initial prestress ($S = 0$).

Step 4—Dynamic stability analysis

The boundaries of the stable and unstable regions (Ince–Strutt maps) are determined by solving Equation (13), which takes the following form:

$$det\left\{ \frac{2EA}{l}\begin{bmatrix} 1 & 0 \\ 0 & 0 \end{bmatrix} + \frac{2S}{l}\begin{bmatrix} 1 & 0 \\ 0 & 1 \end{bmatrix} + \left(1 \pm \frac{1}{2}\frac{P_t}{P}\right)\frac{N(P)}{l}\begin{bmatrix} 0 & 0 \\ 0 & 1 \end{bmatrix} - \frac{\theta^2}{4}\frac{2\rho Al}{3}\begin{bmatrix} 1 & 0 \\ 0 & 1 \end{bmatrix}\right\} = 0 \quad (27)$$

Solving Equation (27) leads to obtaining two resonance frequencies:

$$\eta_1 = \frac{1}{\pi}\sqrt{\frac{3\left[S + \left(1 \pm \frac{1}{2}\,v\right)N(P)\right]}{\rho Al^2}}, \quad \eta_2 = \frac{1}{\pi}\sqrt{\frac{3(EA + S)}{\rho Al^2}}. \quad (28)$$

The first resonant frequency $(28)_1$ depends on both the initial prestress level S and the longitudinal force caused by the load $N(P)$: (23) or (24). In turn, the second resonant frequency $(28)_2$ does not depend on both the longitudinal force caused by the load $N(P)$ and the initial prestress S (for real structures, the values of prestressing forces S are much lower than those of the longitudinal stiffness $S \ll EA$). This means that only one main unstable region can be identified. This is because the structure is characterized by one infinitesimal mechanism.

3. Results for the Simplest Two-Dimensional Cable Structure

First, to illustrate the behavior of structures characterized by the self-stress state and infinitesimal mechanism, dynamic instability is analyzed. Three values of load are considered, i.e., $P = \{1\,\text{kN}, 3\,\text{kN}, 5\,\text{kN}\}$. Cables with diameter $\phi = 20$ mm and length $l = 1$ m are assumed. In turn, the material characteristics of steel, i.e., Young's modulus and density ρ, are 210 GPa and 7860 kg/m^3, respectively.

In this case, the minimum level of initial prestress does not depend on external loads, so $S_{min} = 0$ is assumed. In turn, the maximum level of initial prestress for such data equals $S_{max} = 70$ kN and corresponds to the effort of the structure $W_{max} = 0.85$. Assuming geometric and mechanical characteristics, the values of prestressing forces S are much lower than the longitudinal stiffness EA: $S_{max} = 0.07$ MN $< EA = 66$ MN.

The influence of the initial prestress level S and load on the main unstable region is shown. For example, Figure 4 shows the boundaries for three levels of initial prestress, i.e., $S_{min} = 0$ kN, $S = 30$ kN, and $S_{max} = 70$ kN. As can be seen, independent of the value of the prestress, the size of the regions mostly depends on the load. The greater the load, the larger the region. At the same time, the larger the load, the higher the frequency. The introduction of prestress (Figure 4b,c) decreases the size of the unstable regions and increases the resonant frequencies. The initial prestress level has a greater influence on the size of the unstable regions when smaller loads are applied. For example, in the case of $P = 1$ kN, introducing $S_{max} = 70$ kN results in an overlapping of the boundaries of unstable regions (Figure 4c).

To better compare the influences of the initial prestress level S and the load, Figure 5a shows the areas of unstable regions $A_\eta(S)$. Different behaviors are observed depending on the value of the load. In the case of $P = 1$ kN, the chart displays an almost exponential function. In turn, in the cases of $P = 3$ kN and $P = 5$ kN, the charts show similar behaviors. Comparing the load of $P = 5$ kN with $P = 1$ kN, the area of the unstable regions is larger by 1.7 (at $S = 0$ kN), 3.0 (at $S = 30$ kN), and 8.9 (at $S = 70$ kN) times. In turn, comparing the load of $P = 5$ kN with $P = 3$ kN, the area of the unstable regions is larger by 1.2 (at $S = 0$ kN), 1.3 (at $S = 30$ kN), and 1.7 (at $S = 70$ kN) times.
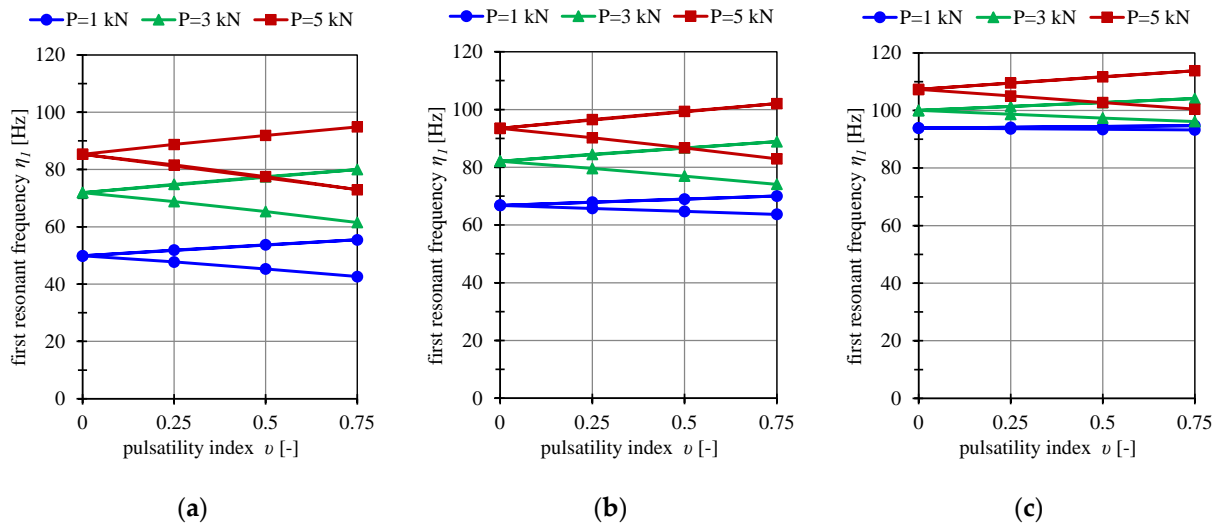
Figure 4. Limits of the main unstable region when (**a**) $S_{min} = 0$ kN; (**b**) $S = 30$ kN; (**c**) $S = 70$ kN.
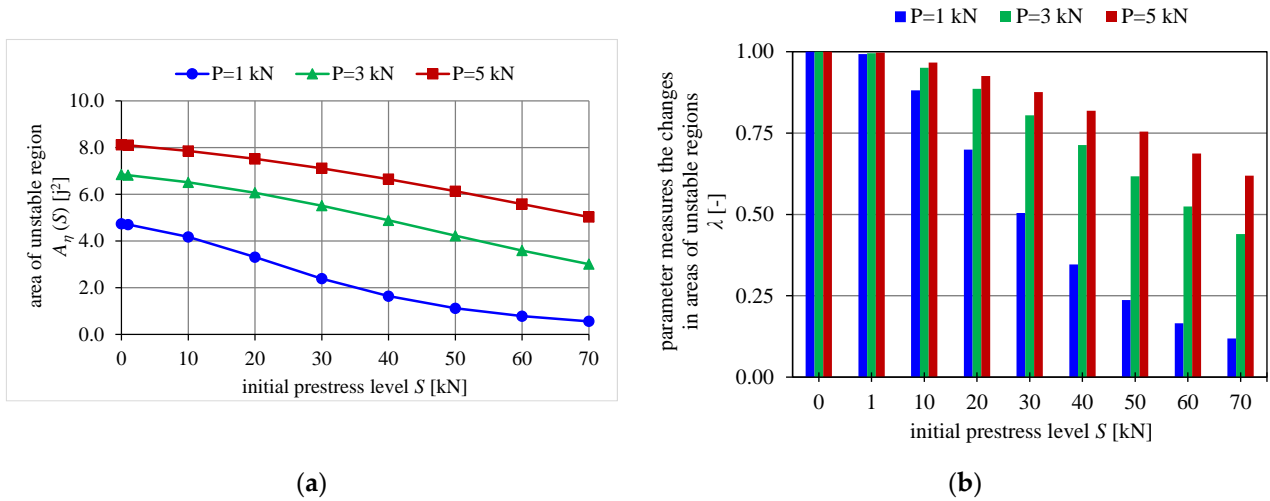

Figure 5. Influence of the initial prestress level S on the (**a**) area of unstable regions A_η, (**b**) range of unstable regions.

To measure the changes in the areas of the unstable regions, the dimensionless parameter λ (15) was calculated (Figure 5b). In the case of $P = 1$ kN, the parameter λ is equal: $\lambda = 0.88$ (at $S = 10$ kN), $\lambda = 0.7$ (at $S = 30$ kN), and $\lambda = 0.12$ (at $S = 70$ kN), which mean that the unstable regions are, respectively, 12%, 30%, and 88% smaller than in the absence of initial prestress ($S = 0$ kN). In turn, in the case of $P = 5$ kN, the unstable regions for the considered prestress levels as previous are smaller by 3% ($\lambda = 0.97$), 8% ($\lambda = 0.92$), and 38% ($\lambda = 0.62$). As can be seen, load causes differences in the changes in parameter λ with growth in the initial prestress level. For $P = 1$ kN, parameter λ decreases almost exponentially; in turn, for $P = 5$ kN, it is a polynomial of the second degree.

4. Results and Discussion for Geiger Domes

The dynamic instability of Geiger domes was analyzed. Particularly, the influence of the initial prestress level on the shape and range of unstable regions was analyzed. This analysis is cognitive in nature. The assumed load is sufficient for evaluating the behavior of domes under periodic excitations. The behaviors of different design solutions known from the literature were compared. The aim of the analysis was to answer the question as to which type of design solution is more sensitive to the risk of excitation vibrations.

4.1. Design Solutions of Geiger Domes

The geometry of a Geiger dome consists of uniformly distributed, flat, load-bearing girders. Domes with six load-bearing girders were analyzed. Two variants of the geometry of the load-bearing girders were considered, i.e., with a closed upper section, type A (Figure 6a), and an open upper section, type B (Figure 6b). Additionally, two designs—regular (Figure 7a,b) and modified (Figure 7c,d)—were taken into account. This means that four different small-scale steel Geiger dome design solutions were compared, i.e., regular type A dome [6,10], regular type B dome [4,5,7–9,17,30,31], modified type A dome [15,16,31], and modified type B dome [32]. Their comparison in terms of the natural frequency range was the subject of our previous study [18].
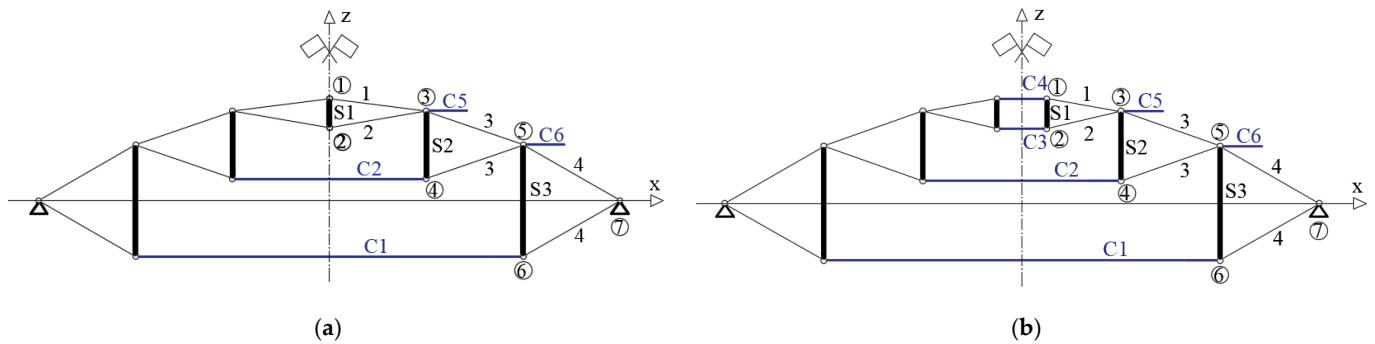

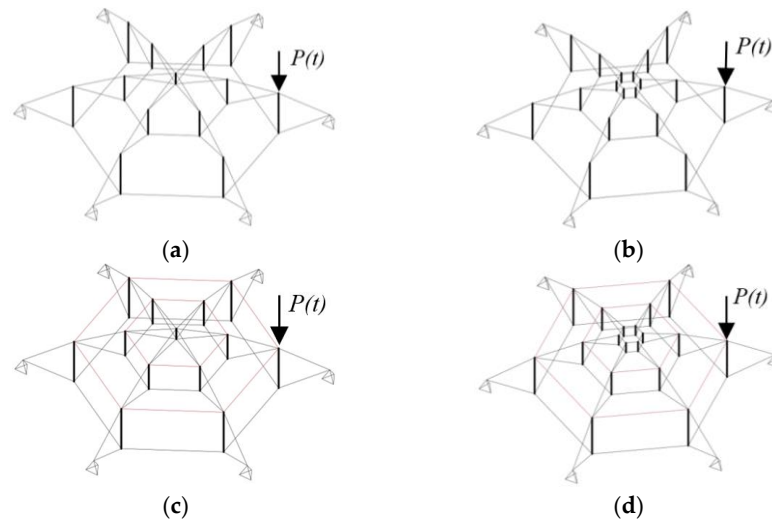**Figure 6.** Load-bearing girders of a Geiger dome: (**a**) type A; (**b**) type B.

Figure 7. Geiger domes: (**a**) regular type A; (**b**) regular type B; (**c**) modified type A; (**d**) modified type B.

The load-bearing girders (Figure 6) consisted of tensioned cables (elements: 1, 2, 3, 4) and compressed struts (elements: S1, S2, S3), which were connected by circumferential cables (elements: C1, C2, C3, C4). In the case of modified solutions, additional circumferential cables C5 and C6 were added to connect the upper nodes. The node coordinates of the load-bearing girders are presented in Table 1. The small-scale steel domes were analyzed. The domes' diameter was 12 m, and their height was 3.25 m. The domes were supported at each external node of the lower section. Three translational degrees of freedom ere taken away. This type of support corresponds to a circumferential clamping ring. It was assumed that the cables were made of S460N steel. Type A cables with a Young modulus $E_e = 210$ GPa [33] were used. The struts were made of S355J2 steel with a Young modulus $E_e = 210$ GPa. The density of steel is equal to $\rho_e = 7860$ kg/m^3. The material and geometrical characteristics are presented in Table 2. The load-bearing capacity was calculated by

taking into account a partial factor for structural resistance. In the case of struts (made with a cold-finished circular hollow section), the load-bearing capacity depends on length l.

Table 1. Node coordinates of the load-bearing girders.

No. of Node		1	2	3	4	5	6	7
type A	x [m]	0.0	0.0	2.0	2.0	4.0	4.0	6.0
type B		0.5	0.5					
types A, B	z [m]	2.1	1.5	1.85	0.45	1.15	−1.15	0.0

Table 2. Material and geometrical characteristics of elements.

Elements	Diameter ϕ [mm]	Thickness t [mm]	Cross-Sectional Area A [m^2]	Moment of Inertia I [m^4]	Load-Bearing Capacity N_{Rd}		
cables	20.0	−	3.14·10^{-4}	7.85·10^{-9}	110.2 kN		
struts	76.1	2.9	6.67·10^{-4}	4.47·10^{-7}	$l = 0.6$ m	$l = 1.4$ m	$l = 2.3$ m
					224.3 kN	170.5 kN	107.1 kN

The calculations were performed with the use of a non-linear model implemented in a proprietary program written in the Mathematica environment.

4.2. Inherent Features of Geiger Domes

The results of the qualitative analysis, which determined the inherent features of Geiger domes, are shown in Table 3. The considered structures are qualitatively different. As can be seen, regular domes are characterized by one self-stress state, whereas modified domes are characterized by three. In the first case, the self-stress state correctly identifies the appropriate normal forces in the structural elements and stabilizes all mechanisms (the self-stress state is appropriate). In the second case, none of the identified self-stress states are appropriate. Due to this, a superimposed self-stress state is necessary. The values of the appropriate self-stress forces $\mathbf{y}_S$ are shown in Table 4. These values were normalized in such a way that the force in the longest strut (**S3**) is equal to −1.

Table 3. Results of the qualitative analysis of Geiger domes.

	No. of			
	Nodes	Elements	Mechanisms	Self-Stress States
Regular type A dome	32	61	18	1
Regular type B dome	42	78	31	1
Modified type A dome	32	73	8	3
Modified type B dome	42	90	21	3

Table 4. Values of the self-stress state $\mathbf{y}_S$ of Geiger domes.

	Regular Geiger Domes		Modified Geiger Domes	
	Type A	Type B	Type A	Type B
el.	$\mathbf{y}_S$ [-]	$\mathbf{y}_S$ [-]	$\mathbf{y}_S$ [-]	$\mathbf{y}_S$ [-]
S1	−0.3804	−0.0845	−0.2277	−0.0506
S2	−0.3043	−0.3043	−0.2646	−0.2646
S3	−1.0000	−1.0000	−1.0000	−1.0000
1	0.5112	0.5142	0.3060	0.3076
2	0.3678	0.3721	0.2201	0.2225

Table 4. *Cont.*

	Regular Geiger Domes		Modified Geiger Domes	
	Type A	Type B	Type A	Type B
3	0.9213	0.9213	0.8010	0.8010
4	2.0061	2.0061	2.0061	2.0061
C1	1.7391	1.7391	1.7391	1.7391
C2	0.8696	0.8696	0.7560	0.7560
C3	-	0.3623	-	0.2167
C4	-	0.5072	-	0.3034
C5	-	-	0.2356	0.2356
C6	-	-	0.2270	0.2270

4.3. Unstable Regions

The periodic force applied to one upper node in the vertical direction (see Figure 7) was taken into account. A constant part of the load $P = 5$ kN was assumed. The impact of the initial prestress S on the limits of the main unstable regions in the plane of parameters v (pulsatility index) and η (resonance frequency) (14) was investigated. The pulsatility index v in the range of 0 to 0.75 was considered, and the impact of the initial prestress S on the resonance frequencies η was investigated. In order to compare the behaviors of all domes, the same maximum prestress level $S_{\max} = 50$ kN was adopted (the maximum cable effort was $W_{\max} = 0.95$ for domes with a closed upper section (domes type A) and $W_{\max} = 0.93$ for domes with an open upper section (domes type B). In turn, the minimum prestress level S_{min} is an individual characteristic of every dome. Type B domes have a lower value $S_{\min} = 2$ kN, whereas type A domes have a much higher value. $S_{\min} = 24$ kN for a regular dome, and $S_{\min} = 35$ kN for a modified dome.

The main unstable regions corresponding to various frequencies depending on the initial prestress were determined. The four main selected unstable regions are presented in this paper. The influence of three levels of initial prestress S on the shape and range of these regions was determined. At this point, it should be noted that in the case of type B domes, the number of frequencies, depending on the initial prestress level S, corresponded to infinitesimal mechanisms. In turn, in case of type A domes, there were three additional frequencies that depended on the prestress [18].

4.3.1. Domes with an Open Upper Section (Type B)

The regular type B dome was characterized by 31 infinitesimal mechanisms, while the modified type B dome had 21. Therefore, 31 and 21 main unstable regions were determined, respectively. For regular domes, the main unstable regions corresponding to the following resonance frequencies are shown: $\eta1$, $\eta10$, $\eta20$, and $\eta31$ (Figure 8), while for the modified dome, they are $\eta1$, $\eta7$, $\eta14$, and $\eta21$ (Figure 9). Three cases of initial prestress, i.e., $S_{min} = 2$ kN, $S = 15$ kN, and $S = 35$ kN, are presented.

Comparing the Ince–Strutt maps with the stable and unstable regions for both domes, similarities are apparent. First, the area of the unstable regions is larger at higher frequencies. Second, at $S_{min} = 2$ kN (Figures 8a and 9a), the unstable regions are larger than those at $S = 15$ kN (Figures 8b and 9b). In turn, at $S = 35$ kN (Figures 8c and 9c), the boundaries of the unstable regions practically coincide. This means that the resonance frequencies η do not depend on the pulsatility index v, and the risk of the excitation of unstable motion decreases.
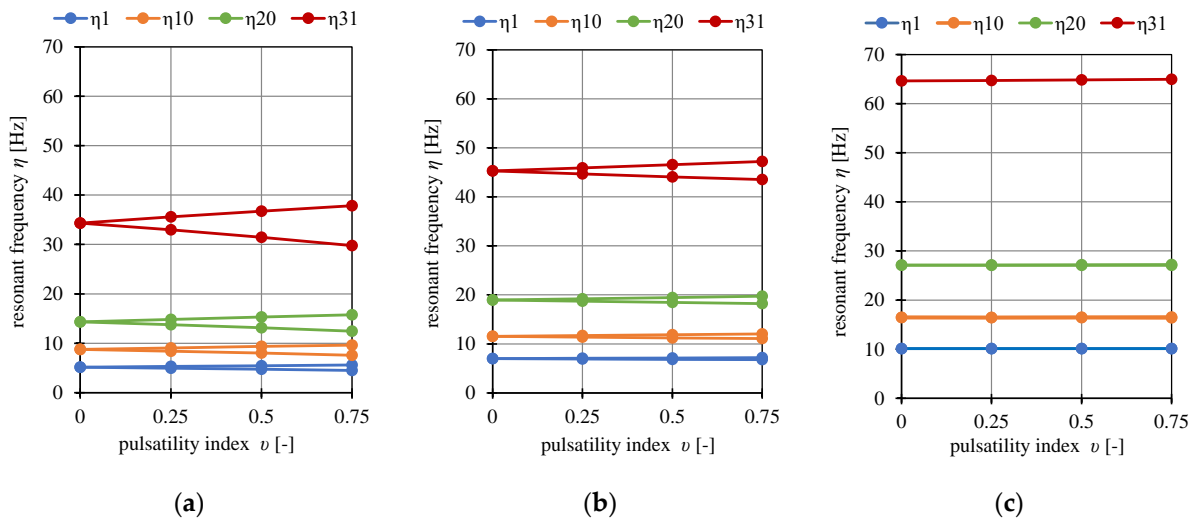
Figure 8. Limits of the four main selected unstable regions of the regular type B dome: (**a**) $S_{min} = 2$ kN; (**b**) $S = 15$ kN; (**c**) $S = 35$ kN.
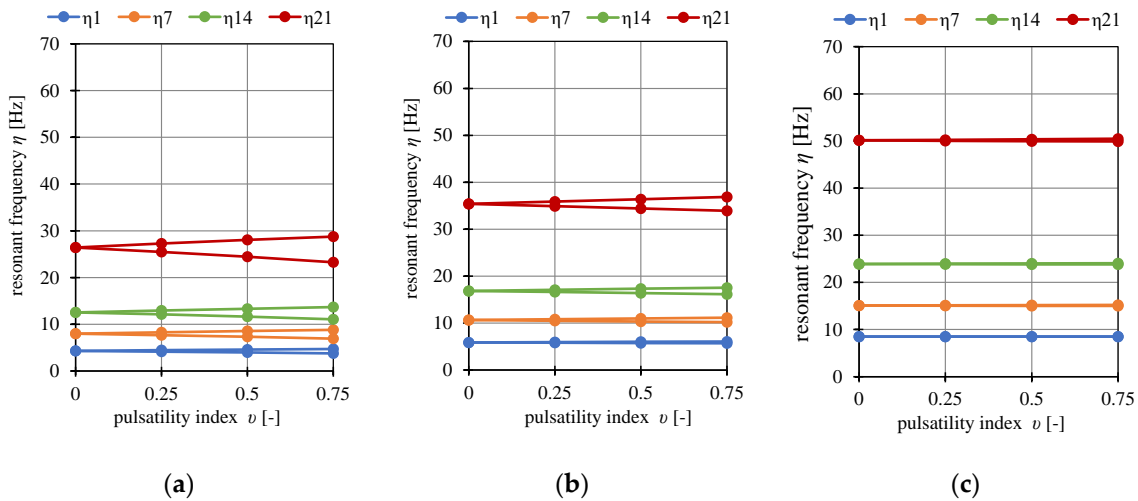

Figure 9. Limits of the four main selected unstable regions of the modified type B dome: (**a**) $S_{min} = 2$ kN; (**b**) $S = 15$ kN; (**c**) $S = 35$ kN.

Differences are also apparent. In the case of a regular dome (Figure 8), the resonance frequencies η are higher, and the unstable regions for the same level of initial prestress S are larger than those of a modified dome (Figure 9). To compare the behavior of the domes, the influence of the initial prestress S on the area of unstable regions $A_\eta(S)$ is shown in Figure 6. As can be seen, at low values of initial prestress ($S \in< 2$ kN; 20 kN >), the area of the unstable regions of a regular dome (Figure 10a) is greater than that of a modified dome (Figure 10b). For example, for the lowest prestress level $S_{min} = 2$ kN, the areas of the unstable region corresponding to the first and last resonance frequencies are larger by 14% and 47%, respectively. However, further compression significantly narrows the unstable areas, and the areas are similar for both domes.
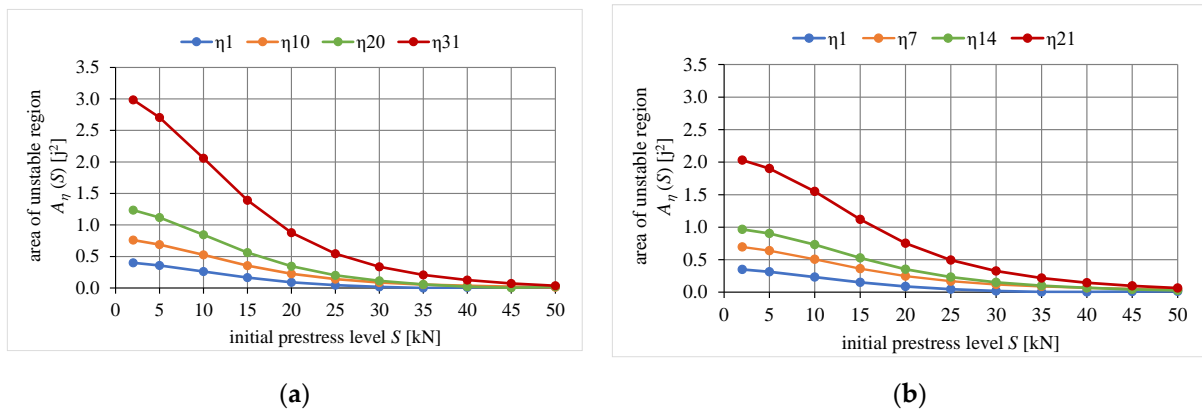
Figure 10. Influence of the initial prestress level S on the area of unstable regions A_η: (**a**) regular type B dome; (**b**) modified type B dome.

The influence of the initial prestress level S on the distribution and range of unstable regions was measured by the nondimensional parameter λ (15) (Figure 11). In the case of the regular dome (Figure 11a), as the initial prestress level increases, the changes in the range of areas are greater. For example, at $S = 15$ kN, the areas are smaller by approximately 53% than the areas at the minimum prestress level, while in the case of the modified dome (Figure 11b), they are about 45% smaller. Parameter λ decreases exponentially as the initial prestress level increases for both domes, and at the maximum level, $\lambda = 0.02$ and $\lambda = 0.04$ (the unstable regions decrease by 98% and 96%). As can be seen, the changes in the range of unstable regions corresponding to almost all resonance frequencies are comparable between the domes, except for the first region (this region corresponds to the first resonance frequency $\eta 1$).
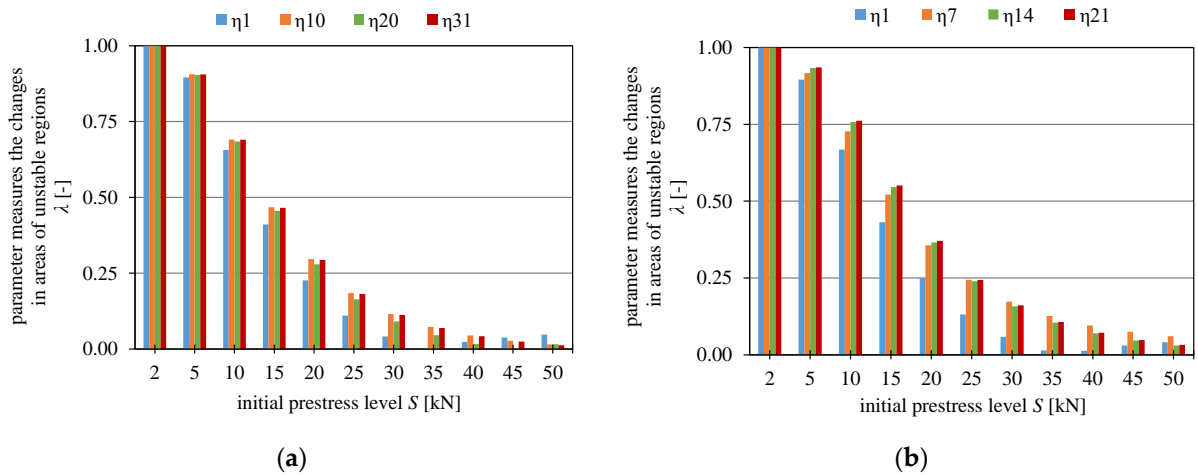

Figure 11. Influence of the initial prestress level S on the range of unstable regions: (**a**) regular type B dome; (**b**) modified type B dome.

As was stated earlier, the unstable regions are the greatest at the lowest prestress level $S_{min} = 2$ kN. In this case, if all the main unstable regions were determined, i.e., 31 for the regular and 21 for the modified dome, the regions would overlap. For example, in Figure 12, the limits of all the main unstable regions of the modified type B dome in the case of the minimal prestress level are shown (the black line marks the rest of the regions, except for those selected: $\eta 1$, $\eta 7$, $\eta 14$, $\eta 21$).
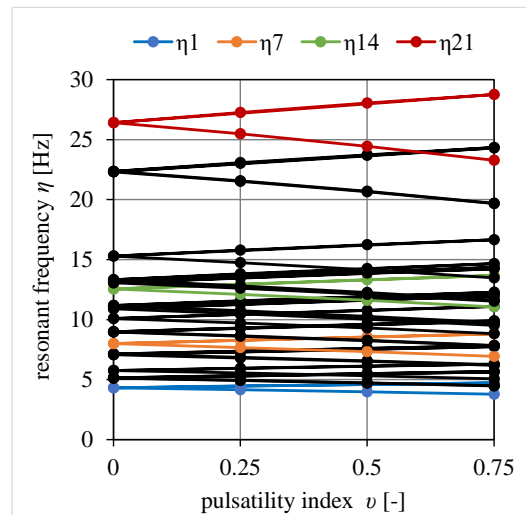
Figure 12. Limits of all main unstable regions of the modified type B dome in the case of the minimal prestress level $S_{min} = 2$ kN.

It should be noted that the next resonance frequencies (like natural frequencies), i.e., $\eta > \eta 32$ and $\eta > \eta 22$, for regular and modified domes, respectively, are independent of the pulsatility index v ($\eta(v = 0 \div 0.75) = $ const.) and of the initial prestress level S (Table 5). The relative increase is less than 1% for all frequencies. These resonance frequencies are twice as high as the natural frequencies.

Table 5. Frequencies [Hz] of type B Geiger domes.

	Regular				Modified			
	Resonance frequency η [Hz]							
	$\eta 32$	$\eta 33$	$\eta 34$	$\eta 35$	$\eta 22$	$\eta 23$	$\eta 24$	$\eta 25$
S_{min}	83.8	180.4	180.9	180.9	81.5	143.9	144.0	169.3
S_{max}	84.2	181.3	181.3	181.3	81.8	144.4	144.4	170.0
Relative increase	0.5%	0.5%	0.2%	0.2%	0.4%	0.3%	0.3%	0.4%
	Natural frequency f [Hz]							
	$f32$	$f33$	$f34$	$f35$	$f22$	$f23$	$f24$	$f25$
S_{min}	41.9	90.1	90.4	90.4	40.7	71.9	71.9	84.6
S_{max}	42.1	90.6	90.6	90.6	40.9	72.1	72.1	85.0
Relative increase	0.5%	0.6%	0.2%	0.2%	0.5%	0.3%	0.3%	0.5%

4.3.2. Domes with a Closed Upper Section (Type A)

The regular type A dome was characterized by 18 infinitesimal mechanisms, while the modified type B dome had 8. This means that 18 and 11 main unstable regions were determined, respectively. However, in this type of dome, there are three additional frequencies depending on the initial prestress. The influences of the initial prestress level on the resonance frequencies are shown in Figures 9 and 10 and Table 6.

For regular domes, the main unstable regions corresponding to the following resonance load frequencies are shown: $\eta 1$, $\eta 6$, $\eta 12$, and $\eta 18$ (Figure 13), while for the modified dome, they are $\eta 1$, $\eta 3$, $\eta 5$, and $\eta 8$ (Figure 14). Three cases of initial prestress were considered, i.e., $S_{min} = 24$ kN, $S = 35$ kN, and $S = 45$ kN for regular domes and $S_{min} = 35$ kN, $S = 40$ kN, and $S = 45$ kN for modified domes.

Table 6. Frequencies of type A Geiger domes.

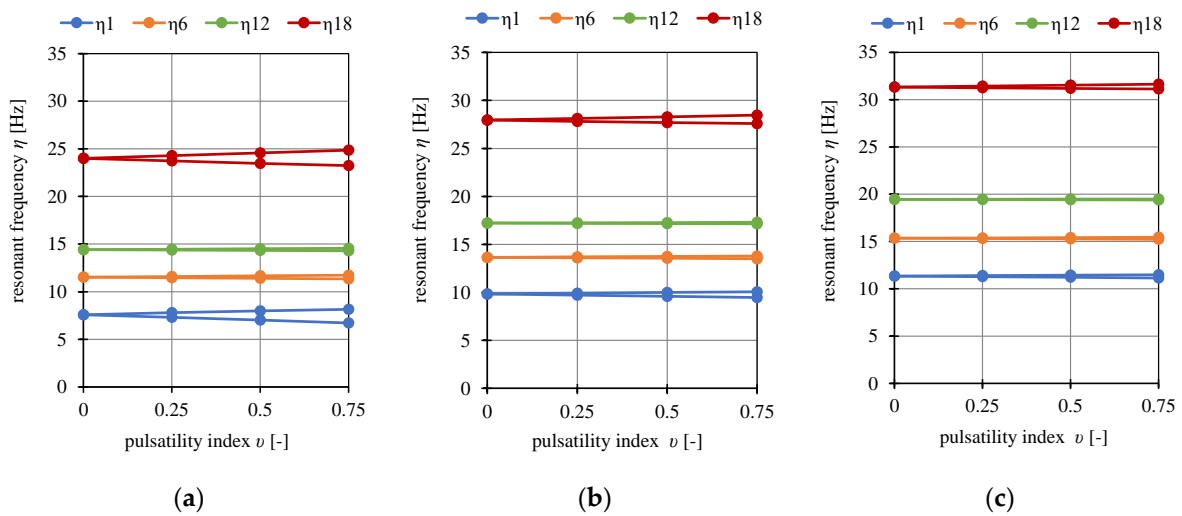|	Regular				Modified			
	Resonance frequency η [Hz]							
	$\eta 19$	$\eta 20$	$\eta 21$	$\eta 22$	$\eta 9$	$\eta 10$	$\eta 11$	$\eta 12$
S_{min}	31.4	31.6	34.8	88.6	30.7	31.0	35.2	85.4
S_{max}	36.7	36.9	41.2	88.8	33.4	33.6	38.6	85.5
Relative increase	16.9%	16.8%	18.4%	0.2%	8.8%	8.4%	9.7%	0.1%
	Natural frequency f [Hz]							
	$f 19$	$f 20$	$f 21$	$f 22$	$f 9$	$f 10$	$f 11$	$f 12$
S_{min}	15.7	15.7	17.3	44.3	15.4	15.4	17.7	42.7
S_{max}	18.4	18.4	20.6	44.4	16.8	16.8	19.3	42.7
Relative increase	17.2%	17.2%	19.1%	0.2%	9.1%	9.1%	9.0%	0.0%

(**a**) (**b**) (**c**)

Figure 13. Limits of the four main chosen unstable regions for the regular type A dome: (**a**) S_{min} = 24 kN; (**b**) S = 35 kN; (**c**) S = 45 kN.

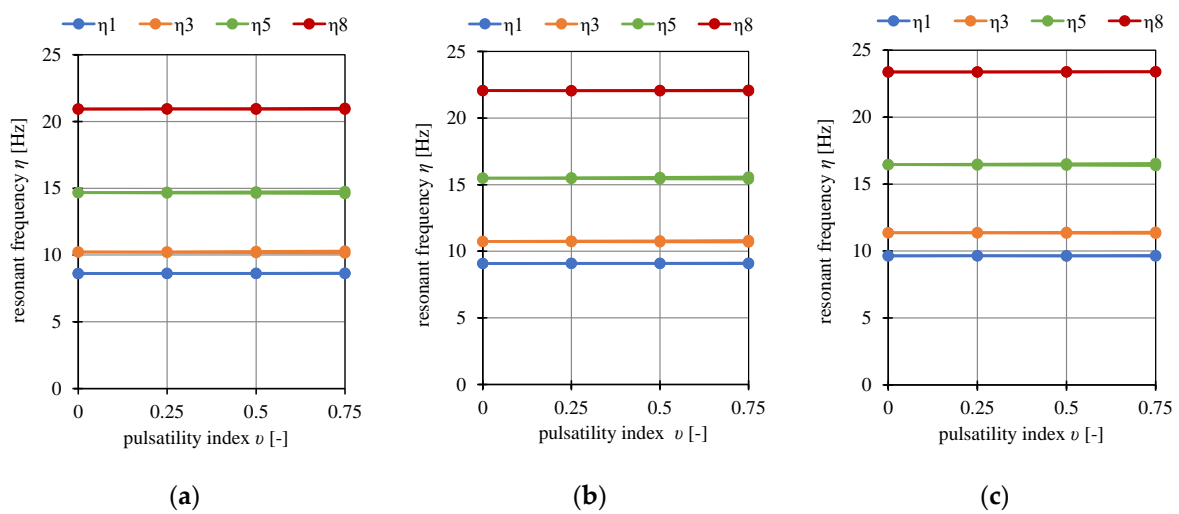(**a**) (**b**) (**c**)

Figure 14. Limits of the four main chosen unstable regions for the modified type A dome: (**a**) S_{min} = 35 kN; (**b**) S = 40 kN; (**c**) S = 45 kN.

The behavior of type A domes is quite different from that of type B domes. This is due to the minimum prestress level, which is much greater. There is also no similarity

between the behaviors of regular and modified type A domes. In the case of regular domes, the areas of unstable regions do not depend on the frequencies (Figure 13), e.g., for $S_{min} = 24$ kN, the areas corresponding to the first $\eta 1$ and eighteenth $\eta 18$ resonance frequencies are comparable, $A_{\eta 1} = 0.54 \ j^2$ and $A_{\eta 18} = 0.62 \ j^2$, whereas for the second resonance frequency $\eta 2$, this is $A_{\eta 2} = 0.15 \ j^2$. There is no rule except one that applies to all four domes: as the initial prestress level S increases, the resonant frequencies also increase, and the range of the unstable regions decreases.

In turn, modified type A domes are not sensitive to the pulsatility index v (Figure 14). The boundaries of the instabilities practically coincide, as in the cases of type B domes for $S \geq 35$ kN.

Analyzing the results obtained for the additional three resonant frequencies (Table 6: $\eta 19$, $\eta 20$, $\eta 21$ for a regular dome and $\eta 9$, $\eta 10$, $\eta 11$ for a modified dome), it can be seen that these frequencies do not depend on the pulsatility index v ($\eta(v = 0 \div 0.75) = $ const.). The boundaries of instabilities coincide; however, these frequencies depend on the initial prestress level S. The regular domes are more sensitive to the initial prestress. The relative increase vs. S_{min} is approximately 16.8–18.4%, while for the modified domes, it is approximately 8.4–9.7%. It should be noted that the behavior of the resonance frequencies is similar to the behavior of the natural frequencies.

In turn, as in the case of type B domes, the next resonance frequencies, i.e., $\eta > \eta 21$ and $\eta > \eta 11$, for regular and modified domes, respectively, are independent of the pulsatility index v and of the initial prestress level S (Table 6). The relative increase is less than 1% for all frequencies. These resonance frequencies are twice as high as the natural frequencies.

5. Conclusions

This study examined the influence of the initial prestress level on the shape and range of unstable regions of small-scale steel Geiger domes. The behavior depends on the design of the dome, which affects the minimum prestress level. Four different design solutions, known from the literature, were compared, i.e., regular and modified domes with closed (type A) and open (type B) upper sections. Type A domes require a much higher initial prestress level to ensure the appropriate distribution of normal forces in the elements than type B domes. In the first case, the minimum prestress levels are 48% and 70% of the maximum prestress level for regular and modified domes, respectively, while in the second case, it is only 4%.

The main unstable regions corresponding to the frequencies depending on the initial prestress were determined. The four selected main unstable regions were presented in this paper. The influence of three initial prestress levels S on the shape and range of these regions was determined. At this point, it should be noted that in the case of type B domes, the number of frequencies, depending on the initial prestress level S, corresponds to infinitesimal mechanisms. In turn, in the case of type A domes, there are three additional frequencies that depend on the prestress. However, for these frequencies, the boundaries of instabilities coincide.

The dynamic stability analysis showed that type B domes are characterized by wider unstable regions than type A domes. In the case of type A domes, unstable regions occur only at low values of initial prestress and completely narrow with the increase in the initial prestress level. In turn, for type B domes, the impact of the initial prestress is weaker. The number of unstable regions depends on the number of infinitesimal mechanisms. Type B domes are characterized by a larger number of infinitesimal mechanisms and thus a larger number of unstable regions. Additionally, they are concentrated close to each other, and some of them coincide, which results in a higher risk of excitation vibrations. Modified type B domes are the most sensitive to changes in resonant frequencies, whereas modified type A domes are the least sensitive. This means that the additional circumferential cables have a negative impact on the dynamic stability of type B domes. For all domes, as the initial prestress level increases, the resonant frequencies also increase. With a high initial prestress level (approximately 70% of the maximum prestress level), the boundaries of

instability practically coincide, and the risk of the excitation of motion with increasing amplitudes decreases.

The application of tensegrity domes in real structures is a very demanding process. Choosing the initial prestress level in real-world applications is very important; however, it is not easy. The process of optimizing the initial prestress level must be carried out. First, the initial prestress level must ensure an appropriate redistribution of normal forces under actual loading. Second, the load-bearing capacity must be ensured, which means that the allowable stresses must not be exceeded. Third, from the point of view of assessing the dynamics of stability, the risk of the excitation of motion with increasing amplitude must be as low as possible. All these conditions should be taken into account in the optimization process. In addition, in terms of applying these types of structures in real objects, additional analyses must be conducted (including experimental studies). The analyses must include the physical non-linearity of cables and local stability (the local buckling of single elements).

Author Contributions: Conceptualization, P.O.; formal analysis, M.S.; methodology, P.O.; software, M.S.; supervision, P.O.; visualization, M.S.; writing—original draft and editing, P.O. All authors have read and agreed to the published version of the manuscript.

Data Availability Statement: The original contributions presented in the study are included in the article, further inquiries can be directed to the corresponding author.

Conflicts of Interest: The authors declare no conflicts of interest.

References

1. Geiger, D.H. Roof Structure. U.S. Patent 4,736,553, 4 December 1988.
2. Rastorfer, D. Structural Gymnastic for the Olympics. *Architectural Record*, September 1988. Available online: https://www.columbia.edu/cu/gsapp/BT/DOMES/SEOUL/s-struc.html (accessed on 19 August 2024).
3. Yuan, X.; Chen, L.; Dong, S. Prestress design of cable domes with new forms. *Int. J. Solids Struct.* **2007**, *44*, 2773–2782. [CrossRef]
4. Xu, X.; Luo, Y. Form-finding of non-regular tensegrities using a genetic algorithm. *Mech. Res. Commun.* **2010**, *37*, 85–91. [CrossRef]
5. Malerba, P.G.; Patelli, M.; Quagliaroli, M. An Extended Force Density Method for the form finding of cable systems with new forms. *Struct. Eng. Mech.* **2012**, *42*, 191–210. [CrossRef]
6. Ma, Q.; Ohsaki, M.; Chen, Z.; Yan, X. Step-by-step unbalanced force iteration method for cable-strut structure with irregular shape. *Eng. Struct.* **2018**, *177*, 331–344. [CrossRef]
7. Ding, M.; Luo, B.; Pan, J.; Guo, Z. Experimental Study and Comparative Analysis of a Geiger-Type Ridge-Beam Cable Dome Structure. *Int. J. Civ. Eng.* **2018**, *16*, 1739–1755. [CrossRef]
8. Jiang, Z.; Liu, X.; Shi, K.; Zhang, Z. Catenary Equation-Based Approach for Force Finding of Cable Domes. *Int. J. Steel Res.* **2019**, *19*, 283–292. [CrossRef]
9. Chen, L.M.; Huang, K.Y.; Liu, Y.J.; Zeng, Y.H.; Li, Z.B.; Zhou, Y.T.; Dong, S.L. Optimization of Cable Dome Structure Design for Progressive Collapse Resistance. *Appl. Sci.* **2023**, *13*, 2086. [CrossRef]
10. Wu, X.; Deng, H.; Zhu, D. Determination of target modes for monitoring the stiffness of cable domes considering random pretension deviations. *J. Eng. Mech.* **2018**, *144*, 04017178. [CrossRef]
11. Yan, X.; Yang, Y.; Chen, Z.; Ma, Q. Mechanical properties of a hybrid cable dome under non-uniform snow distribution. *J. Constr. Steel Res.* **2019**, *153*, 519–532. [CrossRef]
12. Wu, X.; Xu, S.; Ma, J.; Miao, F. Measuring full static displacements of cable domes based only on limited tested locations. *Appl. Math. Model.* **2020**, *77*, 1054–1064. [CrossRef]
13. Obara, P.; Solovei, M.; Tomasik, J. Qualitative and Quantitative analysis of tensegrity steel domes. *Bull. Pol. Acad. Sci.* **2023**, *71*, 1–8.
14. Volokh, K.Y.; Vilnay, O.; Averbuh, I. Dynamics of Cable Structures. *J. Eng. Mech.* **2003**, *129*, 175–180. [CrossRef]
15. Kim, S.D.; Sin, I.A. A comparative analysis of dynamic instability characteristic of Geiger-typed cable dome structures by load condition. *J. Korean Assoc. Spat. Struct.* **2014**, *14*, 85–91. [CrossRef]
16. Atig, M.; Ouni, M.H.; Kahla, N.B. Dynamic stability analysis of tensegrity systems. *Eur. J. Environ. Civ. Eng.* **2017**, *23*, 675–692. [CrossRef]
17. Qin, W.; Gao, H.; Feng, P.; Xi, Z.; Li, Y. Shaking table experimental investigations on dynamic characteristics of CFRP cable dome. *Eng. Struct.* **2023**, *281*, 115748. [CrossRef]
18. Obara, P.; Solovei, M. Assessment of the impact of the number of girders on the dynamic behaviour of Geiger dome. *Arch. Civ. Eng.* **2023**, *69*, 597–611.
19. Bolotin, V.V. Dynamic Instabilities in Mechanics of Structures. *Appl. Mech. Rev.* **1999**, *52*, R1–R9. [CrossRef]

20. Bolotin, V.V.; Weingarten, V.; Greszczuk, L.B.; Trigoroff, K.N.; Gallegos, K.D.; Cranch, E.T. Dynamic Stability of Elastic Systems. *J. Appl. Mech.* **1965**, *32*, 718. [CrossRef]

21. Mathieu, E. Memoir on the Vibratory Movement of an Elliptical Membrane. *J. Math. Pures Appl.* **1868**, *13*, 137–203.

22. Volmir, A.C. *Stability of Elastic Systems*; Science: Moscow, Russia, 1963.

23. Obara, P.; Gilewski, W. Dynamic Stability of Moderately Thick Beams and Frames with the Use of Harmonic Balance and Perturbation Methods. *Bull. Pol. Acad. Sci. Tech. Sci.* **2016**, *64*, 739–750. [CrossRef]

24. Garus, S.; Garus, J.; Sochacki, W.; Nabialek, M.; Petru, J.; Borek, W.; Sofer, M.; Kwiaton, P. Influence of material distribution and damping on the dynamic stability of Bernoulli-Euler beams. *Bull. Pol. Acad. Sci. Tech. Sci.* **2023**, *71*, e145567. [CrossRef]

25. Obara, P.; Tomasik, J. Dynamic Stability of Tensegrity Structures—Part II: The Periodic External Load. *Materials* **2023**, *16*, 4564. [CrossRef] [PubMed]

26. Obara, P.; Tomasik, J. Parametric analysis of tensegrity plate-like structure: Part 2—Quantitative Analysis. *App. Sci.* **2021**, *11*, 602. [CrossRef]

27. Bathe, K.J. *Finite Element Procedures in Engineering Analysis*; Prentice Hall: New York, NY, USA, 1996.

28. Zienkiewicz, O.C.; Taylor, R.L. *The Finite Element Method: The Basis*; Elsevier Butterworth-Heinemann: London, UK, 2000.

29. Laccone, F.; Malomo, L.; Froli, M.; Cignoni, P.; Pietroni, N. Automatic Design of Cable-Tensioned Glass. *Comput. Graph. Forum* **2020**, *39*, 260–273. [CrossRef]

30. Jia, Y.; Ding, M.; Wang, L.; Luo, B.; Ruan, Y. A Comparative Study on the Stability Performance of the Suspen-Dome, Conventional Cable Dome, and Ridge-Beam Cable Dome. *Buildings* **2023**, *13*, 2019. [CrossRef]

31. Guo, J.; Ding, M.; Wang, L.; Ruan, Y.; Luo, B. Study on the Nonlinear Stability and Parametric Analysis of a Tensile–Beam Cable Dome. *Symmetry* **2023**, *15*, 1690. [CrossRef]

32. Zhang, P.; Feng, J. Initial prestress design and optimization of tensegrity systems based on symmetry and stiffness. *Int. J. Solids Struct.* **2017**, *107*, 68–90. [CrossRef]

33. *EN 1993-1-11: 2006*; Eurocode 3: Design of Steel Structures—Part 1–11: Design of Structures with Tension Components.